Electrochimica Acta 531 (2025) 146330

Contents lists available at ScienceDirect

Electrochimica Acta

journal homepage: www.journals.elsevier.com/electrochimica-acta

The effect of 2-mercaptobenzimidazole concentration on the microstructure and mechanical properties of electrodeposited Cu foils

Che Liu [a,b], Xiangcheng Chen [b], Zhao Cheng [b,*], Lei Lu [b,*]

[a] School of Materials Science and Engineering, University of Science and Technology of China, Shenyang 110016, China
[b] Shenyang National Laboratory for Materials Science, Institute of Metal Research, Chinese Academy of Sciences, Shenyang 110016, China

ARTICLE INFO

Keywords:
Electrodeposited Cu foil
2-mercaptobenzimidazole
Microstructure
Strength and elongation
Electrochemical mechanism

ABSTRACT

Electrodeposited copper foils, essential as current collectors in lithium-ion batteries, face the challenge of achieving high strength. This study demonstrates that the incorporation of 2-mercaptobenzimidazole (MBI) as an electrodeposition additive induces significant modifications in the microstructure of electrodeposited copper foils with a thickness of 9 μm, thereby exerting a substantial influence on their surface quality, mechanical properties, and thermal stability. As the MBI concentration increases, the surface roughness of the copper foils decreases markedly, the grain size becomes significantly refined, and the (220) crystallographic texture becomes more pronounced. Remarkably, the highest tensile strength of 656 MPa is achieved at an MBI concentration of 5 mg/L, coinciding with a peak frequency of nanotwinned grains. After annealing, the copper foils retain a refined microstructure and high strength, demonstrating superior thermal stability compared to those prepared without MBI. Electrochemical experiments were conducted to elucidate the working mechanism of MBI, revealing that MBI not only adsorbs onto the substrate but also forms complexes with cupric ions. Our findings offer valuable insights for the development of high-performance electrodeposited copper foils.

1. Introduction

Copper foils play a pivotal role as current collectors in lithium-ion batteries, acting not only as a link between the anodes and the external circuits but also as mechanical support for the anodes [1–3]. Their exceptional electrical conductivity, mechanical properties, and chemical stability make them indispensable for efficient charge transfer and durable operation [4–9]. Throughout the charging and discharging processes of lithium-ion batteries, the intercalation and deintercalation of lithium ions often cause volumetric changes in the anode materials [10,11]. Consequently, the copper foils, tightly bonded to the anodes, undergo stretching during charging and release of tension during discharging. During high-strain amplitude bending and unbending fatigue tests, copper foils exhibit early surface crack initiation, while lower strain amplitudes make crack initiation more difficult [12]. Hence, high-strength copper foil current collectors, capable of constraining anode volumetric changes, make crack initiation in them less likely during operation. Additionally, under prolonged operation, lower-strength copper foil current collectors tend to wrinkle more due to anode volumetric changes. Such wrinkling significantly affects electrical contact and reduces power density [13]. Therefore, using high-strength copper foils as current collectors in lithium-ion batteries ensures their long-term performance and reliability.

Electrodeposition has been extensively used to prepare copper foils, valued for its cost efficiency, flexibility, and control over foil thickness and microstructure [14–17]. The properties of electrodeposited copper foils are largely determined by several deposition parameters, including the composition of the blank electrolyte, current density, temperature, and electrodeposition additive [18–21]. Within an industrial context, all these parameters, aside from the composition of additives, remain relatively constant. Consequently, the strategic use of additives becomes a key approach in adjusting the mechanical, electrical, and surface properties of electrolytic copper foils.

Additives used in electrodeposition enhance the strength of copper foils primarily by refining their grain size or introducing defects. For instance, by the use of protein powder and poly-2-sulfur-2-propane sodium sulfonate (SPS) as electrodeposition additives, the twin boundary density of copper foils increased from 33.6 % to 63.1 %, consequently elevating the tensile strength of the electrolytic copper foils prepared via direct current electrodeposition from 266 MPa to 373 MPa [22]. Several additives, such as 2-mercaptothiazoline [23], polyacrylamide [24], and gelatin [25], have demonstrated efficacy in enhancing electrolytic

* Corresponding authors.
E-mail addresses: zcheng13s@imr.ac.cn (Z. Cheng), llu@imr.ac.cn (L. Lu).

https://doi.org/10.1016/j.electacta.2025.146330
Received 14 November 2024; Received in revised form 1 April 2025; Accepted 25 April 2025
Available online 8 May 2025

copper foil strength through grain refinement, primarily by increasing electrodeposition overpotential. However, the highly conductive electrolyte and elevated production temperatures used in industrial settings make it challenging for electrodeposition additives to generate sufficient overpotential to significantly enhance the strength of electrodeposited copper foils.

Equally important is the surface quality of copper foil current collectors. Reducing the roughness of electrolytic copper foil can significantly improve the wettability of anode slurry, thereby reducing the interfacial impedance. Poor contact between anodes and the anode slurry increases the risk of corrosion and degrades battery performance. It has been reported that as the surface roughness (Rz) of the copper foil decreased from 3.6 μm to 1.2 μm, the oxidation peak corresponding to the deintercalation process shifted from 0.327 V to 0.276 V, indicating a reduced interfacial impedance [26].

Surface roughness reduction typically involves coordinating multiple additives. A commonly employed strategy is combining SPS with a polymer inhibitor to regulate electrodeposition rates on diverse substrate features [27,28]. Nonetheless, this multi-additive approach complicates the control over additive concentrations during electrodeposition processes [29,30], posing practical challenges in copper foil production. Therefore, producing high-strength electrodeposited copper foil with a smooth surface using a simple additive composition remains a significant challenge in industrial settings.

2-Mercaptobenzimidazole (MBI) is a promising electrodeposition additive, considering its various applications in corrosion inhibition and surface treatment [31–35]. It has been found that MBI significantly enhances the corrosion resistance of various metals by forming a protective film on the metal surfaces [36–38]. These studies underscore the ability of MBI to improve the durability and performance of metal surfaces. Moreover, they implicitly demonstrate MBI's potential as an inhibitor in copper foil electrodeposition to modulate the overpotential.

In this study, 2-Mercaptobenzimidazole (MBI) was introduced as an electrodeposition additive to prepare electrolytic copper foils, aimed at enhancing their overall properties. The investigation systematically explored the influence of MBI concentration on the microstructural features, including grain size, nanotwin fraction, and texture. Mechanical tests were conducted to evaluate the strength and elongation of the copper foils prepared with varying MBI concentrations. Additionally, the surface morphology was thoroughly analyzed, and the surface roughness was measured. The thermal stability of the copper foils was evaluated by comparing the microstructure and mechanical properties before and after heat treatment. Furthermore, electrochemical measurements were employed, offering valuable insights into the intricate working mechanism of MBI. These findings not only contribute to the fundamental understanding of MBI's role in electrodeposition processes but also pave the way for the development of high-performance copper foils.

2. Experimental

9 μm thick copper foils were prepared in an electrolytic cell made of polypropylene using a basic electrolyte composed of 1.35 mol/L Cu^{2+} and 2 mol/L H^{+}. 2-mercapto benzimidazole (MBI) was added to the blank electrolyte in the form of an aqueous solution to adjust its concentration in the electrolyte. The electrodeposition temperature was fixed at 50 °C, and the current density applied was kept at 650 mA/cm^2. The above parameters have been extensively applied in the industrial production of copper foils. The cathode and anode used were pure titanium and iridium-coated titanium, respectively. During electrodeposition, the cathode rotated at 500 rpm to facilitate the mass transport process.

The tensile tests were conducted following the guidelines of the standard IPC-TM-650 2.4.18. A universal testing machine (Instron 68TM-5) was used to conduct the tensile test. The specimen was rectangular in shape and measured 150 mm × 12.7 mm. The strain rate was kept constant at 50 mm/min, while the gauge length was set at 50 mm.

The surface roughness of the matte side of the copper foils was measured using a surface roughness tester (Marsurf M300). Surface morphology on the matte side was characterized using a scanning electron microscope (SEM, FEI Verios 460) in secondary electron imaging mode. Prior to observation, all the samples were sequentially cleaned with 10 % dilute sulfuric acid and deionized water. The three-dimensional surface morphology of the copper foils was characterized using a confocal laser scanning microscope (CLSM, Olympus LEXT OLS410) with a planar resolution of 120 nm and a height resolution of 10 nm. The captured area covered 26 μm × 26 μm. To obtain the cross-sectional microstructure of the copper foils, they were coated with a copper protective layer of approximately 2 mm thickness via electrodeposition and then polished mechanically and electrochemically. The electropolishing was conducted at ambient temperature using an electrolyte consisting of phosphoric acid (25 %), alcohol (25 %), and deionized water (50 %). The cross-sectional images of the copper foils were obtained using the SEM in backscattering electron imaging mode. The intercept method was employed to determine the average grain size by statistically measuring around 300 grains. The grain size refers to the lateral dimension of the grains, which is perpendicular to the growth direction of the copper foil. Electron backscattered diffraction (EBSD) was scanned by a SEM (FEI Nova 450) with a step size of 80 nm and under a voltage of 20 kV. A transmission electron microscope (TEM, FEI Tecnai F20) was used to capture bright-field images for a detailed examination of the substructures of the copper foils. The TEM specimens were circular with a diameter of 3 mm, attached to a copper ring of the same size, and then thinned with twin-jet electrochemical polishing in an electrolyte of phosphoric acid (20 %) and methanol (80 %) at approximately −20 °C. The thinning was conducted parallel to the growth direction of the copper foils. Based on the TEM images, the volume fraction of grains containing nanotwins in each copper foil sample was estimated. X-ray diffraction (XRD, Bruker D8 A) was utilized to determine the crystal structure and calculate the texture coefficient (TC) of the matte side of the copper foils. The TC formula is expressed as follows:

$$TC(hkl) = \frac{I(hkl)}{I_0(hkl)} \Big/ \frac{1}{n}\sum_{hkl}\frac{I(hkl)}{I_0(hkl)} \quad (1)$$

Where TC (hkl) represents the texture coefficient of a particular (hkl) plane, I(hkl) denotes the measured relative intensity, I_0(hkl) signifies the relative intensity derived from standard powder diffraction as provided by the JCPDS data, and n stands for the total number of diffraction peaks taken into account. The radiation source utilized is Cu Kα (λ = 1.5418 Å), and scanning in the 2θ range is conducted from 20° to 100° at a scanning rate of 1.5°/min.

The copper foils underwent a heat treatment process within an atmospheric box furnace at 200 °C for 10 min. The evaluation of the copper foils' thermal stability involved characterizing the microstructure of the annealed samples and examining their mechanical properties.

The electrochemical measurements were conducted in a conventional three-electrode cell made of glass with an electrochemical workstation (Metrohm VIONIC). The Electrochemical analyses were performed with a blank electrolyte comprising 0.5 mol/L Cu^{2+} and 2 mol/L H^{+} at 25 °C. The employment of an electrolyte with reduced Cu^{2+} concentration and lower temperature markedly enhanced the resolution and sensitivity of the electrochemical measurements performed in this study. A platinum plate counter electrode and mercury (I) sulfate reference electrode (MSE) were utilized. All the working electrode potentials E used in this paper refer to the reference electrode. A glassy carbon rotating disk electrode (GC-RDE) with a diameter of 3 mm was employed as the working electrode. Before each measurement, 7 μm thick copper was electrodeposited onto the working electrode surface with the blank electrolyte, making a copper working electrode. The rotating speed of the working electrode was kept constant at 100 rpm in

each measurement. LSV was performed by negative sweeping from open circuit potential to E = −1.1 V at a rate of 5 mV/s. Anodic dissolution experiments were also started from an open circuit potential at a rate of 20 mV/s. Electrochemical impedance spectroscopy (EIS) was conducted at E = −0.65 V with an amplitude of 10 mV in the frequency range from 100 kHz to 0.05 Hz.

3. Results

3.1. Surface morphology and microstructure evolution with MBI concentration

Fig. 1 presents the surface morphology and roughness of copper foils prepared with varying concentrations of MBI, ranging from 0 ppm to 15 ppm. At 0 ppm (Fig. 1(a)), the crystallites appear rounded with no obvious faceting, displaying a mixture of large and small crystallites. Upon increasing the MBI concentration to 5 ppm (Fig. 1(b)), the surface morphology reveals an abundance of smaller crystallites, and some of the large crystallites are covered with much smaller ones. At 10 ppm MBI (Fig. 1(c)), the surface morphology becomes flattened, while at 15 ppm (Fig. 1(d)), nearly all crystallites show faceting, with most assuming a triangular prism geometry, aligned such that one lateral face is parallel to the substrate surface. As shown in Fig. 1(e), Ra and Rz serve as metrics for assessing the surface roughness of the copper foils. Increasing MBI concentration in the electrolyte from 0 ppm to 5 ppm results in a significant reduction in the Rz value, dropping from 1.93 μm to a low of 1.02 μm. Further increasing the concentration to 15 ppm leads to an even lower Rz of 0.76 μm. These findings highlight the critical role of MBI in modulating the nucleation process, leading to a remarkable enhancement in the surface quality of the copper foils.

To further evaluate the surface roughness and morphology of the copper foils, the three-dimensional (3D) surface morphology and the corresponding root mean square roughness values S_q are presented in Fig. 2(a–d). The results reveal a progressive decrease in surface roughness with increasing MBI concentration. The copper foil prepared without additive exhibits the highest roughness, with an S_q of 0.315 μm, characterized by densely distributed protrusions with pronounced height variations. In contrast, the copper foils prepared with 5 ppm and 10 ppm MBI display comparable surface morphologies, featuring less prominent protrusions and a more refined surface texture. The foil prepared with 15 ppm MBI, which has the lowest roughness (S_q = 0.216 μm), presents the smoothest surface among the four samples. The 3D morphology reveals a flatter topography with minimal height variations, resulting in a more compact and uniform surface.

The line profiles extracted from the 3D surface data (Fig. 2(e–h)) further illustrate the surface-smoothing effect of MBI. The profile of the copper foil prepared without MBI (Fig. 2(e)) shows pronounced and erratic height variations, indicative of a rough surface. In contrast, the foil prepared with 15 ppm MBI (Fig. 2(h)) exhibits a stable and uniform profile with minimal fluctuations, confirming the enhanced surface smoothness achieved with higher MBI concentrations.

Fig. 3(a-d) presents cross-sectional SEM images illustrating the microstructures of copper foils prepared with a range of MBI concentrations. In the absence of MBI (Fig. 3(a)), the copper foil exhibits a heterogeneous microstructure with a mixture of large and small grains. As the MBI concentration increases to 5 ppm (Fig. 3(b)), there is a noticeable refinement of the grain structure. The grains appear more uniform and smaller in size than the MBI-free sample, suggesting that MBI promotes the formation of finer and more homogeneous grains. Further increasing the MBI concentration to 10 ppm and 15 ppm (Fig. 3 (c) and (d)) continues to show a refined grain structure; the grain structures remain fine and relatively uniform, similar to the microstructures observed at 5 ppm. The average grain sizes for the copper foils are summarized in Fig. 3(e). The addition of 5 ppm MBI significantly reduces the average grain size from 394 nm at 0 ppm to 200 nm. Further increasing the MBI concentration to 10 ppm and 15 ppm results in a moderate reduction in grain sizes, with average grain sizes of 178 nm and 172 nm. It is apparent that MBI serves as an effective grain refiner, significantly reducing the average grain size of the copper foils.

Fig. 3 (f-i) exhibits the bright field transmission electron microscopy (TEM) images of the copper foils, providing further insights into the microstructural changes caused by MBI. Fig. 3(f) displays a relatively coarse microstructure without observable twin structures. As the concentration of MBI increases (Fig. 3(g-i)), a reduction in grain size is observed, alongside the emergence of twin structures. The volume fraction of grains containing nano-twins for each sample is depicted in Fig. 3(j). The fraction markedly rises from 2.7 % at 0 ppm MBI to 13.6 % at 5 ppm MBI, before experiencing a slight reduction with further increases in MBI concentration. Evidently, the electrodeposition condition facilitated by MBI proves conducive to twin formation.

Fig. 4(a) illustrates the XRD patterns of the matte side of the copper foils, with the diffraction peaks of three key crystallographic orientations ((111), (200), (220)) clearly identified. The data reveals that as the concentration of MBI rises, there is a significant enhancement in the intensity of the (220) peak, whereas the intensity of the (111) peak experiences a notable decrease. Fig. 4(b) depicts the changes in the texture coefficients associated with varying MBI concentrations. Starting at 1.63 at 0 ppm, the (220) texture coefficient remains relatively constant up to 5 ppm. With further increases in MBI concentration, there is a sharp increase in the preference for the (220) orientation, with the coefficient rising to 2.39 at 10 ppm and peaking at 2.77 at 15 ppm. In contrast, the (111) and (200) orientations exhibit different trends. The results demonstrate that the crystallographic texture of copper foils can be significantly altered by MBI. As the concentration of MBI increases,

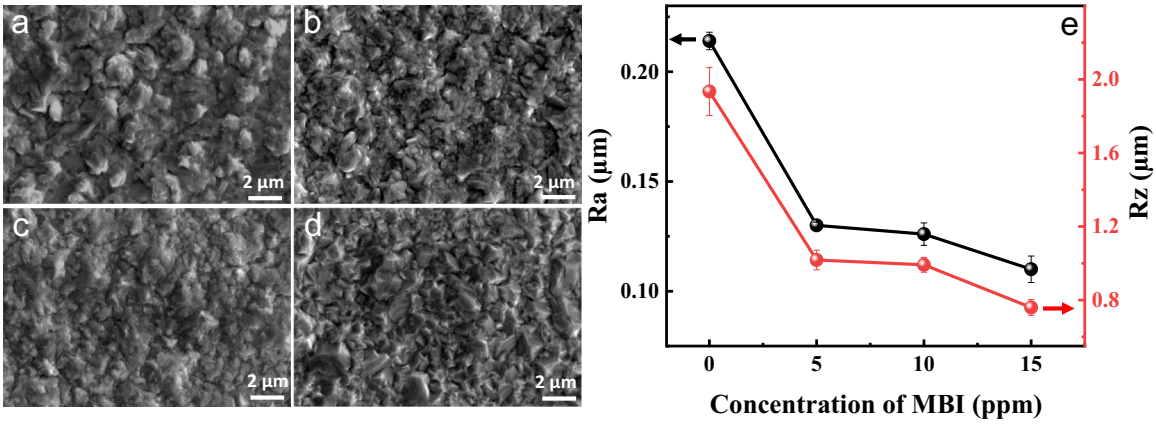

Fig. 1. . (a–d) Surface morphologies of copper foils prepared with varying concentrations of MBI: (a) 0 mg/L, (b) 5 mg/L, (c)10 mg/L, (d) 15 mg/L. (e) Surface roughness of the copper foils.

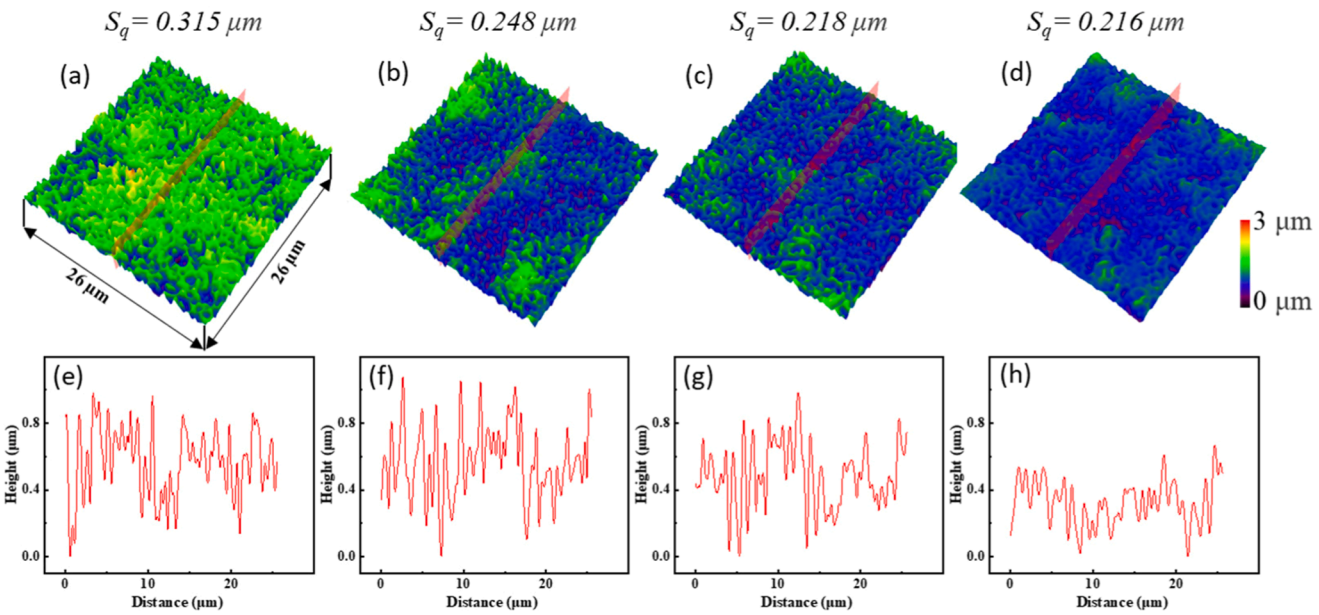

Fig. 2. . 3D surface morphologies (26 μm × 26 μm) of copper foils electrodeposited with MBI concentrations of 0 mg/L (a), 5 mg/L (b), 10 mg/L (c), and 15 mg/L (d). The cross-sectional profiles corresponding to (a), (b), (c), and (d) are shown in (e), (f), (g), and (h). respectively.

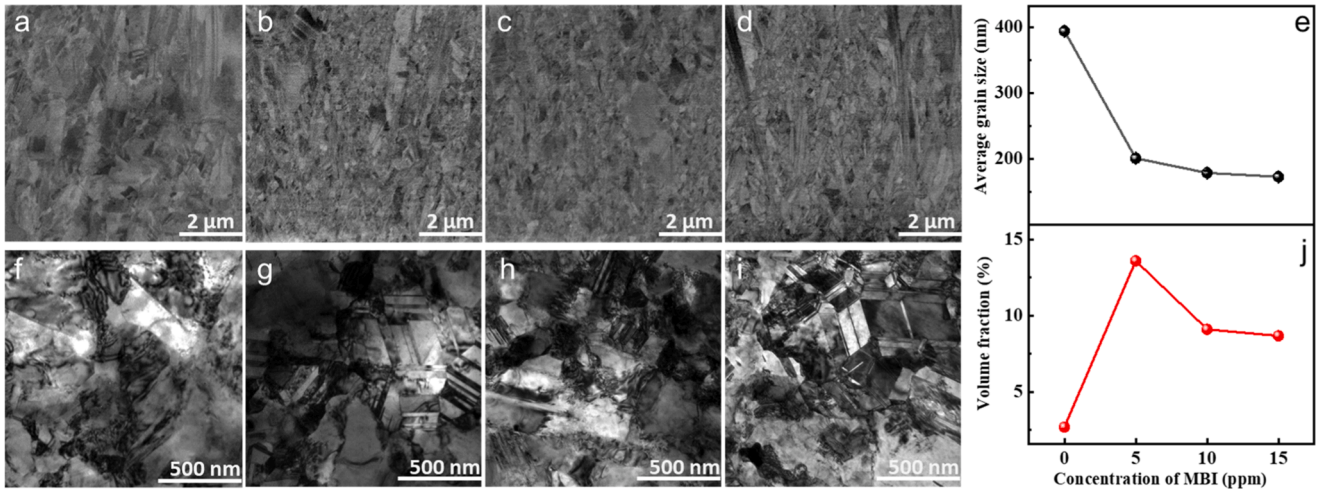

Fig. 3. . (a–d) Cross-sectional SEM images and (f-i) TEM bright-field images showing the microstructures of copper foils prepared with varying concentrations of MBI: (a, f) 0 mg/L, (b, g) 5 mg/L, (c, h) 10 mg/L, (d, i) 15 mg/L. (e) Average grain size of the copper foils. (j) Volume fraction of twin-containing grains of the copper foils.

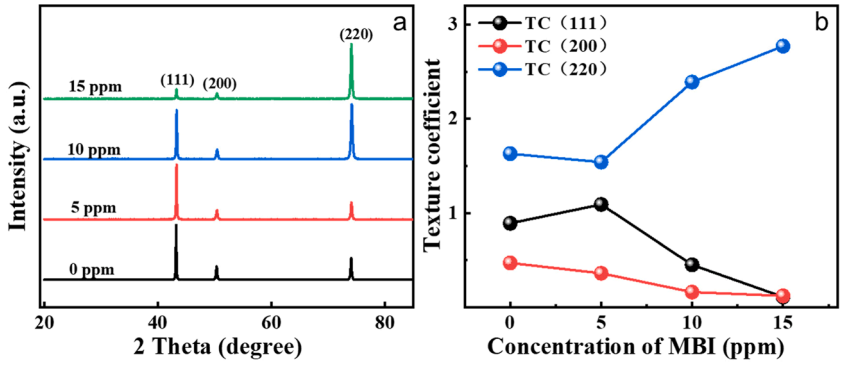

Fig. 4. . (a) XRD patterns and (b) texture coefficients of copper foils prepared with varying concentrations of MBI.

there is a notable promotion of the (220) orientation, while the (111) and (200) orientations are suppressed.

Fig. 5 presents the EBSD results of the copper foil samples. Fig. 5(a1-d1) displays the orientation maps, Fig. 5(a2-d2) shows the inverse pole figures (IPF). The IPF maps reveal a gradual increase in the {110} crystallographic orientation with increasing MBI concentration, which is consistent with the X-ray diffraction (XRD) results, confirming a preferential growth along the {110} plane. The orientation maps demonstrate that the addition of MBI significantly refines the grain structure. The samples prepared with MBI exhibit finer and more fragmented grains, whereas the copper foil prepared without additives displays a coarser microstructure.

Overall, the introduction of MBI induces a distinct structural modification compared to the additive-free sample, resulting in a finer microstructure and enhancing the preferential growth along the {110} orientation.

3.2. Mechanical properties

Fig. 6(a) presents four representative tensile stress-strain curves of copper foils prepared with different concentrations of MBI. The addition of MBI as an electrodeposition additive clearly leads to an enhancement in the tensile strength of the copper foils. Fig. 6(b) demonstrates the tensile strength and elongation of the copper foils. Remarkably, when the MBI concentration increases from 0 ppm to 5 ppm, there is a marked enhancement in the tensile strength of the copper foil, quantified by a significant elevation from 551 MPa to 656 MPa. However, as the MBI concentration continues to rise, the tensile strength gradually declines, measuring 635 MPa at 10 ppm MBI and 590 MPa at 15 ppm MBI. The elongation exhibited by the copper foils follows a similar trend with increasing MBI concentration. The elongation increases from 3.1 % at 0 ppm MBI to 3.6 % at 5 ppm MBI but then decreases to 2.6 % and 2.2 % at 10 ppm and 15 ppm MBI, respectively. An optimal concentration of 5 ppm MBI has been identified for producing copper foils with superior mechanical properties. The tensile strengths of the copper foils prepared with MBI are compared with those reported in previous literature [7,21, 22,24,25,39–45], as shown in Fig. 6(c). The tensile strengths achieved in this study are markedly higher than those in other studies, particularly at 5 ppm MBI, demonstrating the effectiveness of MBI in strengthening copper foils.

3.2.1. Thermal stabilities

Fig. 7(a-d) presents cross-sectional SEM images illustrating the microstructure of copper foils, which were fabricated with varying concentrations of MBI and subsequently annealed at 200 °C for 10 min. Fig. 7(a) shows the annealed microstructure of the copper foil prepared without MBI, displaying predominantly large and irregularly shaped grains. Notably, a single large grain extends through the entire thickness of the copper foil—a phenomenon not observed in the other samples. As the MBI concentration increases to 5 ppm (Fig. 7(b)), the grains become considerably finer. This trend continues with further increases in MBI concentration, as shown in Fig. 7(c) and (d) for 10 ppm and 15 ppm MBI, respectively. The average grain size of both annealed and as-deposited samples is presented in Fig. 7(e). The copper foil prepared without MBI exhibits the most significant grain growth during annealing, increasing by 293 nm to reach a final size of 687 nm. In contrast, after annealing, the foil prepared with 5 ppm MBI shows minimal change, with grain size rising by 175 nm to 376 nm. The copper foils prepared with 10 and 15 ppm MBI display comparable grain growth, resulting in final annealed grain sizes of 430 nm and 423 nm, respectively. The copper foils prepared with MBI exhibit a more stable microstructure at elevated temperatures, as indicated by the moderate increase in grain size, in contrast to the pronounced grain growth observed in the copper foil prepared without MBI.

Fig. 8(a) presents four representative tensile stress-strain curves of the annealed copper foils. The post-annealing tensile strength of the copper foils prepared with MBI remains superior to that of the copper foil prepared without MBI. Fig. 8(b) presents the tensile strength and elongation of the annealed copper foils. The tensile strength of the copper foil prepared with the blank electrolyte drops significantly to 427 MPa following the heat treatment. In stark contrast, the annealed copper foil prepared with 5 ppm MBI still exhibits outstanding mechanical properties, achieving a tensile strength of 583 MPa. In comparison, copper foils produced with 10 ppm and 15 ppm MBI have slightly lower post-thermal treatment tensile strengths, measuring 548 MPa and 552 MPa, respectively. Overall, the copper foils prepared with MBI demonstrate superior thermal stability compared to the copper foil prepared with the blank electrolyte. This stability is most evident in the copper foil prepared with 5 ppm MBI, which shows minimal grain size growth and the highest tensile strength after annealing.

4. Discussion

The experimental results above demonstrate that MBI is not only effective as a grain refiner but also promotes the formation of nanotwins, significantly altering the microstructure and surface morphology of the copper foils. Consequently, the copper foils prepared with MBI exhibit exceptional mechanical properties combined with superior thermal stability. To fully grasp the extent of MBI's influence, it is imperative to uncover its working mechanism. The subsequent section delves deeply

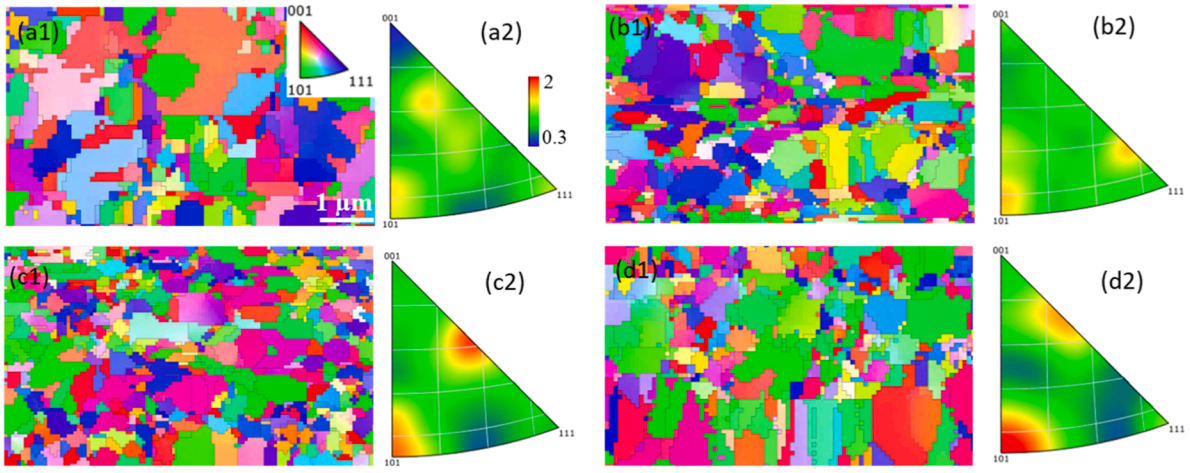

Fig. 5. . (a1–d1) Orientation maps and (a2-d2) corresponding inverse pole figures (IPF) of copper foils prepared with various MBI concentrations: (a1, a2) 0 mg/L, (b1, b2) 5 mg/L, (c1, c2)10 mg/L, (d1, d2) 15 mg/L.

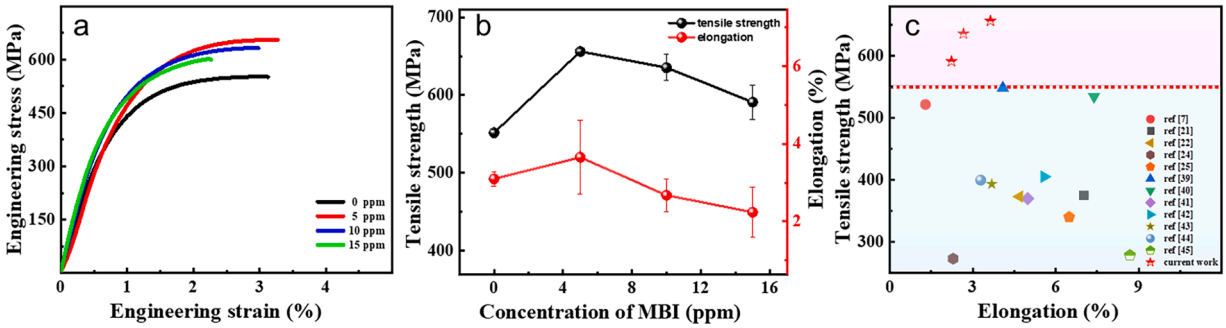

Fig. 6. . (a) Tensile stress-strain curves and (b) tensile strength and elongation of copper foils prepared with varying concentrations of MBI. (c) Comparison of tensile strengths from the present work with recent studies [7,21,22,24,25,39–45].

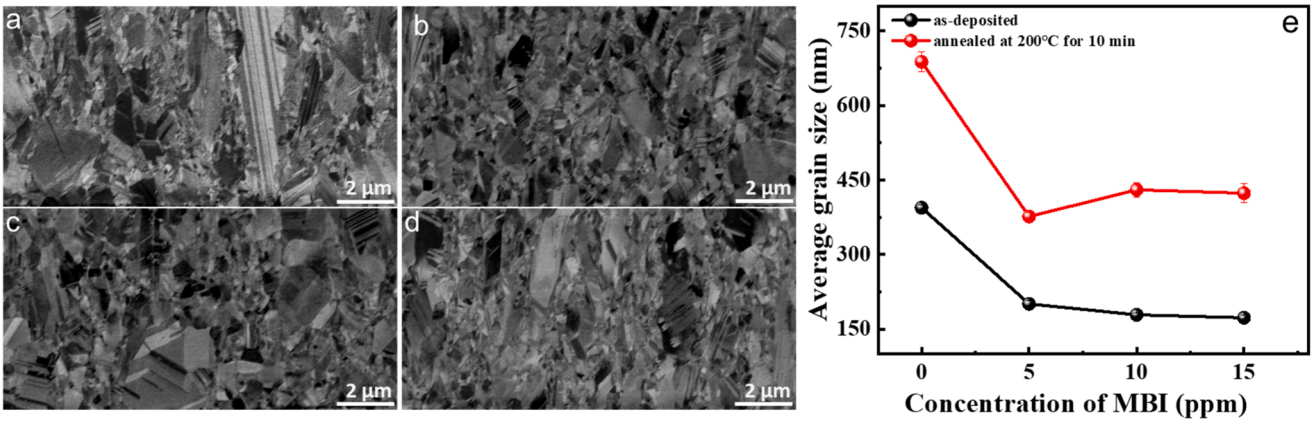

Fig. 7. . (a–d) Cross-sectional SEM images of copper foils prepared with varying concentrations of MBI and annealed at 200 °C for 10 min: (a) 0 mg/L, (b)5 mg/L, (c) 10 mg/L, (d) 15 mg/L. (e) Comparison of average grain sizes between as-deposited and annealed copper foils prepared with varying concentrations of MBI.

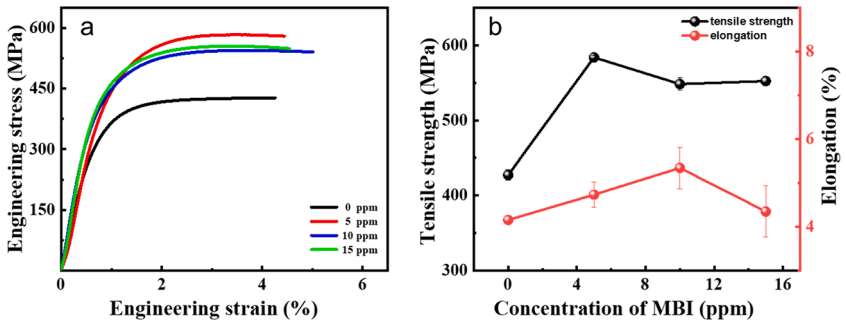

Fig. 8. . (a) Tensile stress-strain curves and (b) tensile strength and elongation of copper foils prepared with varying concentrations of MBI and annealed at 200 °C for 10 min.

into the working mechanism of MBI, aided by a series of electrochemical analyses. Additionally, it explores the impact of MBI as an electrodeposition additive on nucleation mechanisms. It also elucidates the relationship between the improved properties and the microstructure regulated by MBI.

4.1. Electrochemical analysis

The linear sweep voltammetry (LSV) curves, representing the electrolyte with varying concentrations of MBI, are illustrated in Fig. 9(a). The LSV curve of the blank electrolyte displays three distinct kinetic stages, which can be differentiated by the working electrode potential E. The first stage spans from E = −0.39 V (open circuit potential) to −0.65 V, wherein the electrode process is governed by the electrode reaction. Transitioning into the second stage, spanning from E = −0.65 V to −0.8 V, mass transport begins to influence the rate of the electrode reaction, resulting in mixed control. Finally, in the third stage, characterized by electrode potentials more negative than E = −0.8 V, mass transport takes complete control, with the current density stabilizing at its limit. Upon the introduction of MBI into the electrolyte, the cupric ion reduction reaction initiates at various working electrode potentials depending on the MBI concentration. Specifically, at 1 ppm, it occurs at E = −0.73 V, while at 3 ppm and 5 ppm, it starts at E = −0.82 V and −0.84 V, respectively. The addition of MBI to the electrolyte notably shifts the reduction potential of cupric ions towards a more negative direction, indicating a hindrance to their reduction process. A higher concentration of MBI further intensifies this hindrance, leading to an even more pronounced negative shift in the reduction potential. In the presence of MBI, as soon as the potential of the working electrode drops below the reduction potential, there is an abrupt increase in the

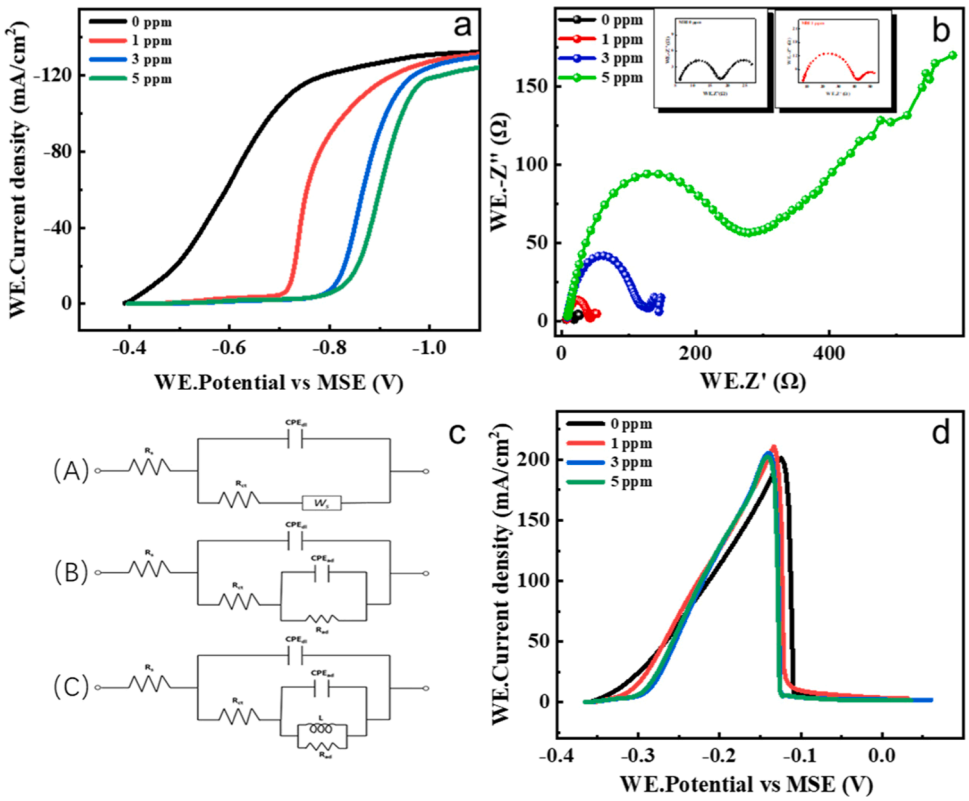

Fig. 9. . Electrochemical analysis at various MBI concentrations. (a) Linear sweep voltammetry, (b) Nyquist plots (Insets show enlarged Nyquist plots at 0 and 1 ppm MBI), and (d) anodic dissolution. (c) Equivalent circuits utilized to fit experimental EIS data at *E*=−0.65V: (A) for 0 and 5 ppm MBI; (B) for 1 ppm MBI; (C) for 3 ppm MBI.

electrode reaction rate, which is followed by the second and third kinetic stages.

The Nyquist plot of the electrolytes at E = −0.65 V is depicted in Fig. 9(b). In the blank electrolyte, this plot exhibits a capacitive loop followed by a straight line, succeeded by a loop. The occurrence of a straight line followed by a loop typifies planar Nernstian diffusion impedance [46]. At a concentration of 1 ppm MBI, the Nyquist plot reveals two distinct capacitive loops, each associated with a specific electrode reaction: the first loop corresponds to the reduction of cupric ions, while the second most likely arises from the electroreduction of substances adsorbed onto the surface of the working electrode. At 3 ppm MBI, the Nyquist plot exhibits a capacitive loop followed by an inductive loop, although it is too distributed to fit. The Nyquist plot of 5 ppm MBI shows a capacitive loop and a Warburg-type diffusion. The equivalent circuits used for fitting the EIS data are depicted in Fig. 9(c), comprising constant phase element CPE, resistance R, and Warburg element Ws, with fitting parameters presented in Table 1. The parameters R_s, R_{ct}, and R_{ad} correspond to the solution resistance, the cupric ion reduction resistance, and the electroreduction resistance of the adsorbed substances, respectively. The capacitances of the cupric ion reduction reaction and the electroreduction reaction are represented by C_{dl} and C_{ad}, respectively. Additionally, the quotient of the effective diffusion thickness squared and the effective diffusion coefficient is denoted as $\tau_{Warburg}$, which represents a key parameter in analyzing mass transport dynamics within the electrochemical system. Both R_s and R_{ct} increase consistently as the MBI concentration rises. R_s shows a slight increase from 5.99 Ω at 0 ppm MBI to 8.05 Ω at 5 ppm MBI, indicating an increased resistance to ion transportation in the electrolytes. R_{ct} increases significantly from 11.29 Ω at 0 ppm MBI to 265.2 Ω at 5 ppm MBI, representing a marked rise in resistance to the cupric ion reduction. Moreover, C_{dl} decreases as MBI concentration increases, dropping from 4.3 μF at 0 ppm MBI to 1.48 μF at 5 ppm MBI. Variation in C_{dl} typically correlates with the adsorption of species on working electrode surfaces.

Table 1
Parameters used for EIS data fitting.

Concentration of MBI (ppm)	R_s (Ω)	C_{dl}(μF)	R_{ct} (Ω)	$\tau_{Warburg}$ (s)	C_{ad}(mF)	R_{ad}(Ω)
0	5.99	4.30	11.29	5.28	—	—
1	7.60	4.14	32.28	—	113.13	15.75
3	7.68	1.87	109.20	—	—	—
5	8.05	1.48	265.20	902	—	—

Fig. 9(d) displays the outcome of anodic dissolution experiments. Initially, the dissolution rate in the blank electrolyte is faster than that in the MBI-containing electrolytes, and the dissolution of the copper electrode is suppressed in the presence of MBI. However, as the working electrode potential becomes more positive, the dissolution rate of the copper electrode in the MBI-containing electrolytes surpasses the dissolution rate in the blank electrolyte.

The negative shift in the cupric ion reduction potential observed in the LSV experiment is primarily due to the significant depletion of free cupric ions in close proximity to the working electrode surface. The availability of free cupric ions is severely limited, with only a minimal concentration remaining accessible for reduction. This scarcity of free cupric ions is intrinsically linked to the molecular structure of the MBI molecule. A distinctive feature of the structure, particularly in the imidazole ring, is that the lone pair of electrons on the nitrogen atom at the 3-position is not involved in conjugation [47], bestowing MBI with a pronounced affinity towards metal cations. This characteristic facilitates the formation of stable complexes between MBI molecules and cupric ions. Additionally, the presence of a mercapto group within the MBI molecule plays a pivotal role; the sulfur atom within this group is known for its specific adsorption capabilities on copper surfaces [48,49]. The adsorption of MBI onto the copper substrate significantly enhances its

complexation effect. In addition, the complexation of MBI molecules with cupric ions contributes to the formation of a more compact MBI film. Together, these two factors impose significant restrictions on the mobility of most cupric ions in the vicinity of the electrode surface. The proposed working mechanism is illustrated in Fig. 10(a). Upon reaching a critical threshold in working electrode potential, the complexation between MBI and cupric ions breaks, leading to the observed burst in the working electrode current density, as shown in Fig. 9(a). Since part of the overpotential still contributes to disrupting the complex formation and overcoming the steric hindrance of MBI molecules, the electrode process is markedly hindered even after the break of the complexation.

The EIS analysis offers compelling validation of the hypothesized behavior of MBI during electrodeposition. The second capacitive loop in the Nyquist plot at 1 ppm MBI likely originates from the electroreduction of MBI molecules that are adsorbed on the substrate surface. At 3 ppm MBI, the appearance of a distributed inductive loop can be attributed to the inclusion or desorption of adsorbed MBI molecules. The irregular and dynamic nature of the inductive loop suggests that MBI coverage is continually fluctuating, albeit at a low magnitude. The pronounced rise in the cupric ion reduction resistance induced by the addition of MBI at $E = -0.65$ V stems from the depletion of free cupric ions near the electrode surface. Additionally, the slight rise in the solution resistance can be explained by the presence of nonadsorbed MBI-cupric ion complexes in the electrolyte.

The results of the anodic dissolution experiment provide further evidence supporting the proposed working mechanism of MBI. The suppressed dissolution rate in the MBI-containing electrolyte at the beginning of the experiment is caused by the specific adsorption of MBI on the copper electrode, which stabilizes it. As cupric ions of the complex are in a lower energy state, the dissolution rate in the MBI-containing electrolytes gradually becomes faster as the electrode potential shifts more positively.

Based on the results of the LSV experiment and the chemical structure of the MBI molecule, a working mechanism is proposed in which MBI adsorbs onto a copper electrode surface and simultaneously forms complexes with cupric ions. The results of the EIS and anodic dissolution experiments further validate the proposed working mechanism.

4.2. Regulatory effect of MBI on nucleation mechanism, surface roughness, and texture

Fig. 1 presents the surface morphology of the copper foils, clearly depicting the size and shape of the surface crystallites, which underscores the significant influence of MBI in controlling the nucleation and growth mechanism. At 0 ppm MBI, the rounded appearance of the crystallites is the result of an isotropic growth rate. Moreover, the surface displays a mixture of large and small crystallites, suggesting concurrent nucleation and growth—a characteristic consistent with progressive nucleation. In contrast, instantaneous nucleation typically results in more uniform crystallite sizes, as all nuclei form at the same time, leading to simultaneous growth [50]. With the addition of 5 ppm MBI, a surge in the number of small crystallites is observed, primarily attributed to the higher nucleation density driven by the increased overpotential. The reduction in the size of the crystallites leads to a notable reduction in the surface roughness of the copper foil prepared at this MBI concentration. Increasing to 10 ppm MBI, the flattened surface morphology implies a suppressed growth rate of the crystallites in the direction perpendicular to the substrate, yielding an even more refined surface. Finally, at 15 ppm MBI, the crystallites predominantly adopt a triangular prism geometry, and the copper foil exhibits the lowest surface roughness. Apart from grain refinement, the decrease in the surface roughness can also be attributed to the geometry of the crystallites formed at 15 ppm MBI, which exhibit a reduced vertical height. The contribution of grain size to the surface roughness of electrodeposits is indeed non-negligible; nonetheless, the influence exerted by the geometry of crystallites merits equal consideration. Despite the addition of MBI, nucleation size heterogeneity persists, confirming that MBI does not fundamentally alter the progressive nucleation mode.

A high concentration of MBI changes the shape of the crystallites to a triangular prism; at the same time, the (220) texture becomes predominant. By integrating the information regarding texture and the geometry of the crystallites, it becomes feasible to identify all the faces of the triangular prism-shaped crystallites crystallographically, as shown in Fig. 10(b). Preferential adsorption of additive molecules induces specific shapes and orientations in electrodeposited crystallites. The presence of additive molecules on specific faces of a crystallite tends to reduce the energy of those faces. Consequently, in an electrodeposition process, the metallic ions prefer to adsorb and undergo reduction on crystallite faces with minimal or no additive molecules. This results in the surfaces, preferentially adsorbed by additive molecules, experiencing the lowest growth rate, typically making them the exposed surfaces of crystallites in equilibrium [19,51]. Thus, a plausible electrocrystallization mechanism influenced by MBI involves the preferential promotion of nuclei with a (220) texture, exposing crystallographic faces of varying orientations, including {200} faces. The selective adsorption of MBI molecules on the {200} surfaces suppresses their growth rate, rendering them the predominant exposed faces and facilitating the expansion of other orientations. This adsorption-driven anisotropic growth contributes to the development of the observed texture.

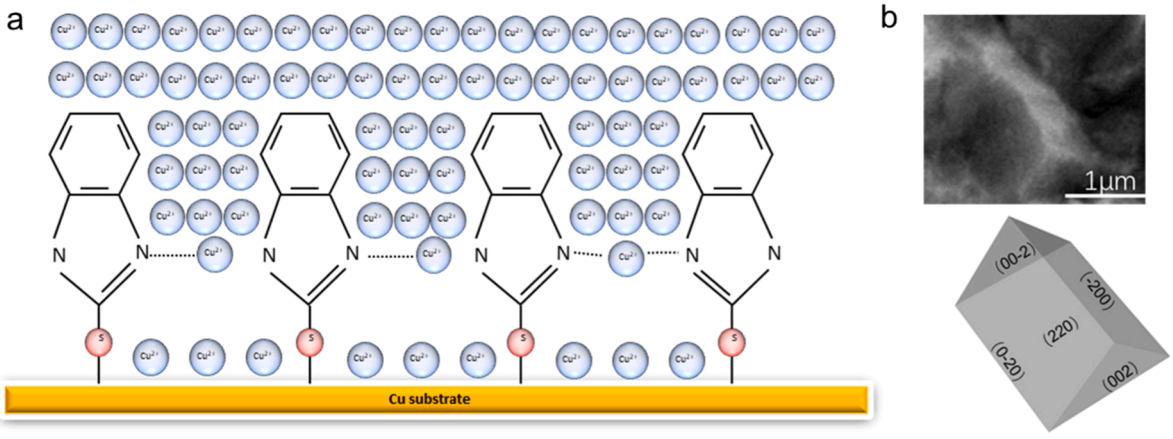

Fig. 10. . (a) Schematic illustration of the working mechanism of MBI; (b) SEM image of a surface crystallite of copper foil prepared with 15 ppm MBI and the crystallographic identification of its surfaces.

4.3. Origin of high strength and enhanced thermal stability

The results of the tensile tests demonstrate that electrolytic copper foils prepared with MBI exhibit significantly enhanced strength. The superior mechanical properties can be attributed to two primary factors. Firstly, the presence of MBI results in pronounced grain refinement by inhibiting the reduction process of cupric ions. Smaller grain sizes correspond to an increased grain boundary area. The grain boundaries act as obstacles to dislocation motion, thereby enhancing the tensile strength of copper foils with finer grains [52,53]. Secondly, MBI facilitates the formation of twins within the copper foils. Twin boundaries also provide resistance to dislocation motion, contributing to higher strength [54,55]. Moreover, the ability of twins to accommodate dislocations inside them [56] suppresses localized plastic deformation, which benefits ductility. Consequently, the copper foil prepared with 5 ppm MBI exhibits superior mechanical performance, combining enhanced tensile strength and elongation among all the samples. This improvement can also be partially attributed to the promotion of (220) texture [57], which is known to contribute to higher strength. However, the grain refinement induced by MBI, while strengthening the foils, may slightly reduce their electrical conductivity due to increased electron scattering at the grain boundaries [58].

The copper foils prepared with MBI also exhibit superior thermal stability. This improved thermal stability can be attributed to the presence of twin boundaries within the copper foils. Twin boundaries are coherent, where atoms across them are arranged more orderly, resulting in a lower energy state [59]. Additionally, twin boundaries, at elevated temperatures, act as effective barriers to diffusion processes that could otherwise lead to grain boundary sliding [60]. By impeding such diffusion, twin boundaries help stabilize grain boundaries, thereby contributing to the improved thermal stability of the copper foils.

5. Conclusion

The copper foils prepared with MBI exhibit significant grain size refinement, along with enhanced twin formation and improved surface quality. These structural enhancements translate into copper foils endowed with outstanding mechanical strength and exceptional thermal stability. The highest tensile strength achieved by the copper foils is 656 MPa, and it remains at 583 MPa even after being annealed at 200 °C for 10 min. The microstructural changes stem from the unique working mechanism of MBI, which not only adsorbs onto the cathode surface but also forms complexes with cupric ions. This interaction significantly enhances the polarization degree of copper foil electrodeposition processes. Moreover, MBI exerts a discernible influence on the nucleation dynamics, promoting the formation of crystallites with triangular prism geometry and (220) orientation. This comprehensive understanding of MBI's role in copper foil production elucidates its potential as an electrodeposition additive for optimizing the overall properties of copper foils.

CRediT authorship contribution statement

Che Liu: Writing – review & editing, Writing – original draft, Methodology, Investigation, Formal analysis, Conceptualization. **Xiangcheng Chen:** Methodology, Investigation, Formal analysis. **Zhao Cheng:** Writing – review & editing, Supervision, Methodology, Investigation, Formal analysis, Conceptualization. **Lei Lu:** Writing – review & editing, Supervision, Resources, Conceptualization.

Declaration of competing interest

The authors declare that they have no known competing financial interests or personal relationships that could have appeared to influence the work reported in this paper.

Acknowledgements

L.L. acknowledges financial support from the National Natural Science Foundation of China (NSFC, Grant Numbers. 92463302, 92163202, U24A2027); the project of Global Common Challenges (172GJHZ2023075GC), Chinese Academy of Sciences (CAS). Z.C. acknowledges financial support from NSFC under Grant Numbers. 52371124 & 52422102 and Youth Innovation Promotion Association, CAS.

Data availability

Data will be made available on request.

References

[1] B. Zhang, D. Li, J. Wan, Dispersed distribution derived integrated anode for lithium ion battery, J. Mater. Sci. Technol. 35 (10) (2019) 2319–2324.
[2] P. Zhu, D. Gastol, J. Marshall, R. Sommerville, V. Goodship, E. Kendrick, A review of current collectors for lithium-ion batteries, J. Power Sources 485 (2021) 229321.
[3] H. Jeong, J. Jang, C. Jo, A review on current collector coating methods for next-generation batteries, Chem. Eng. J. 446 (2022) 136860.
[4] X. Li, M. Zhao, Q. Guo, C. Zhao, M. Ding, D. Zou, Z. Ding, Z. Zhang, M. He, K. Liu, Single-crystallization of electrolytic copper foils, J. Mater. Sci. Technol. 176 (2024) 112–118.
[5] S. Xiong, J. Sun, Y. Xu, X. Yan, Effect of lubricants and annealing treatment on the electrical conductivity and microstructure of rolled copper foil, J. Electron. Mater. 44 (2015) 2432–2439.
[6] S. Zhen, H. Jian, S. Ning, F. Xiaowei, L. Juan, W. Lijuan, T. Yunzhi, T. Yuhui, L. Binghu, L. Dashuang, Effects of the synergistic interaction of Cl^- and organic additives on the organization and properties of copper foil, Nonferrous Met. Sci. Eng. 15 (2) (2024) 220–227.
[7] Y. Wu, C. Wang, H. Han, L. Li, Z. Lai, Y. Hong, S. Wang, G. Zhou, W. He, Y. Chen, Bromine-enhanced polarization for strengthening ultra-thin copper foil in lithium-ion battery, J. Mater. Res. Technol. 30 (2024) 3831–3839.
[8] C. Fear, D. Juarez-Robles, J.A. Jeevarajan, P.P. Mukherjee, Elucidating copper dissolution phenomenon in Li-ion cells under overdischarge extremes, J. Electrochem. Soc. 165 (9) (2018) A1639–A1647.
[9] C.E. Hendricks, A.N. Mansour, D.A. Fuentevilla, G.H. Waller, J.K. Ko, M.G. Pecht, Copper dissolution in overdischarged lithium-ion cells: x-ray photoelectron spectroscopy and X-ray absorption fine structure analysis, J. Electrochem. Soc. 167 (9) (2020) 090501.
[10] S. Yin, Q. Ji, X. Zuo, S. Xie, K. Fang, Y. Xia, J. Li, B. Qiu, M. Wang, J. Ban, Silicon lithium-ion battery anode with enhanced performance: multiple effects of silver nanoparticles, J. Mater. Sci. Technol. 34 (10) (2018) 1902–1911.
[11] Z. Zhou, D. Chaoying, P. Wenchao, L. Yang, Z. Fengbao, X. Fan, One-step fabrication of two-dimensional hierarchical Mn2O3@ graphene composite as high-performance anode materials for lithium ion batteries, J. Mater. Sci. Technol. 80 (2021) 13–19.
[12] H. Merchant, M. Minor, Y. Liu, Mechanical fatigue of thin copper foil, J. Electron. Mater. 28 (1999) 998–1007.
[13] R. Kataoka, Y. Oda, R. Inoue, M. Kitta, T. Kiyobayashi, High-strength clad current collector for silicon-based negative electrode in lithium ion battery, J. Power Sources 301 (2016) 355–361.
[14] L. Liu, Y. Bu, Y. Sun, J. Pan, J. Liu, J. Ma, L. Qiu, Y. Fang, Trace bis-(3-sulfopropyl)-disulfide enhanced electrodeposited copper foils, J. Mater. Sci. Technol. 74 (2021) 237–245.
[15] A. Ibanez, E. Fatas, Mechanical and structural properties of electrodeposited copper and their relation with the electrodeposition parameters, Surf. Coat. Technol. 191 (1) (2005) 7–16.
[16] N. Tantavichet, M.D. Pritzker, Effect of plating mode, thiourea and chloride on the morphology of copper deposits produced in acidic sulphate solutions, Electrochim. Acta 50 (9) (2005) 1849–1861.
[17] M. Hakamada, Y. Nakamoto, H. Matsumoto, H. Iwasaki, Y. Chen, H. Kusuda, M. Mabuchi, Relationship between hardness and grain size in electrodeposited copper films, Mater. Sci. Eng. A 457 (1–2) (2007) 120–126.
[18] T.-G. Woo, I.-S. Park, K.-W. Seol, The effect of additives and current density on mechanical properties of cathode metal for secondary battery, Electron. Mater. Lett. 9 (2013) 535–539.
[19] C.-Y. Fang, D.-P. Tran, H.-C. Liu, J.-J. Ong, Y.-Q. Lin, W.-Y. Hsu, C. Chen, Effect of electroplating current density on tensile properties of nanotwinned copper foils, J. Electrochem. Soc. 169 (4) (2022) 042503.
[20] H.-Y. Cheng, D.-P. Tran, K. Tu, C. Chen, Effect of deposition temperature on mechanical properties of nanotwinned Cu fabricated by rotary electroplating, Mater. Sci. Eng. A 811 (2021) 141065.
[21] H. Chen, K. Chen, Y. Sheng, J. Qu, X. Wang, D. You, D. Shan, Properties and microstructure regulation of electrodeposited ultra-thin copper foil in a simple additive system, Mater. Res. Express 11 (5) (2024) 056405.
[22] J. Han, Y. Wu, K. Zhao, H. Wang, S. Liu, X. Liu, Effects of controlling grain growth mode on microstructures and properties of Cu foil, J. Mater. Res. Technol. 24 (2023) 2018–2027.

[23] Y. Sun, L. Huang, H. Xie, B. Liu, Y. Fang, G. Han, J. Liu, High-strength copper foil prepared with 2-mercaptothiazoline by direct current electrodeposition, Electrochim. Acta 466 (2023) 143068.
[24] S.P. Wang, K.X. Wei, W. Wei, Q.B. Du, I.V. Alexandrov, Enhancing surface roughness and tensile strength of electrodeposited copper foils by composite additives, Phys. Status Solidi A 219 (5) (2022) 2100735.
[25] Y. Liu, N. Song, X. Fan, B. Lu, D. Li, L. Wang, Z. Sun, Y. Tang, Preparation of ultra-thin copper foil with low profile and high tensile strength on surface of 18-μm carrier copper foil, Trans. Indian Inst. Met. (2024) 1–9.
[26] J. Zhang, D. Zuo, X. Pei, C. Mu, K. Chen, Q. Chen, G. Hou, Y. Tang, Effects of electrolytic copper foil roughness on lithium-ion battery performance, Metals (Basel) 12 (12) (2022) 2110.
[27] M. Tan, J.N. Harb, Additive behavior during copper electrodeposition in solutions containing Cl−, PEG, and SPS, J. Electrochem. Soc. 150 (6) (2003) C420.
[28] A. Chrzanowska, R. Mroczka, M. Florek, Effect of interaction between dodecyltrimethylammonium chloride (DTAC) and bis (3-sulphopropyl) disulphide (SPS) on the morphology of electrodeposited copper, Electrochim. Acta 106 (2013) 49–62.
[29] S. Choe, M.J. Kim, H.C. Kim, S.K. Cho, S.H. Ahn, S.-K. Kim, J.J. Kim, Degradation of bis (3-sulfopropyl) disulfide and its influence on copper electrodeposition for feature filling, J. Electrochem. Soc. 160 (12) (2013) D3179.
[30] T.Y. Kim, S. Choe, J.J. Kim, Decomposition of polyethylene glycol (PEG) at Cu cathode and insoluble anode during Cu electrodeposition, Electrochim. Acta 357 (2020) 136803.
[31] G. Xue, Y. Lu, Various adsorption states of 2-mercaptobenzimidazole on the surfaces of gold and silver studied by surface enhanced Raman scattering, Langmuir 10 (3) (1994) 967–969.
[32] G. Xue, X. Huang, J. Ding, Surface reaction of 2-mercaptobenzimidazole on metals and its application in adhesion promotion, J. Chem. Soc., Faraday Trans. 87 (8) (1991) 1229–1232.
[33] S. Guo, G. Xue, Y. Qian, Interfacial modification of polymer/metal joints by a two-component coupling system of polybenzimidazole and 2-mercaptobenzimidazole, Appl. Surf. Sci. 84 (4) (1995) 351–356.
[34] M. Finšgar, 2-Mercaptobenzimidazole as a copper corrosion inhibitor: part II. Surface analysis using X-ray photoelectron spectroscopy, Corros. Sci. 72 (2013) 90–98.
[35] D. Chadwick, T. Hashemi, Electron spectroscopy of corrosion inhibitors: surface films formed by 2-mercaptobenzothiazole and 2-mercaptobenzimidazole on copper, Surf. Sci. 89 (1–3) (1979) 649–659.
[36] H. Lgaz, S. Masroor, M. Chafiq, M. Damej, A. Brahmia, R. Salghi, M. Benmessaoud, I.H. Ali, M.M. Alghamdi, A. Chaouiki, Evaluation of 2-mercaptobenzimidazole derivatives as corrosion inhibitors for mild steel in hydrochloric acid, Metals (Basel) 10 (3) (2020) 357.
[37] P. Morales-Gil, M. Walczak, C.R. Camargo, R. Cottis, J. Romero, R. Lindsay, Corrosion inhibition of carbon-steel with 2-mercaptobenzimidazole in hydrochloric acid, Corros. Sci. 101 (2015) 47–55.
[38] M. Jakeria, L. Ward, I. Cole, Long term durability studies on the corrosion inhibition effect of 2-mercaptobenzimidazole (C3H4N2S) on AA6022: mechanism of film formation and influence of IMPs, Surf. Interfaces 25 (2021) 101164.
[39] L.-p. Wang, Z.-b. Bai, W.-c. Sun, L.-l. Du, X.-l. Peng, Y. Xiao, J. Zhang, Y.-p. Jia, S.-m. Du, H. Cai, Effect of low temperature annealing on microstructure and properties of copper foil, Mater. Today Commun. 36 (2023) 106617.
[40] J. Zhang, H. Chen, B. Fan, H. Shan, Q. Chen, C. Jiang, G. Hou, Y. Tang, Study on the relationship between crystal plane orientation and strength of electrolytic copper foil, J. Alloys Compd. 884 (2021) 161044.
[41] W. Yu, C. Lin, Q. Li, J. Zhang, P. Yang, M. An, A novel strategy to electrodeposit high-quality copper foils using composite additive and pulse superimposed on direct current, J. Appl. Electrochem. 51 (2021) 489–501.
[42] Y. Li, G. Huang, X. Yin, X. Chen, X. Ma, Y. Li, E. Yao, Effect of copper ion concentration on microstructure and mechanical properties of electrolytic copper foil. IOP Conference Series: Materials Science and Engineering, IOP Publishing, 2018 012166.
[43] R. Zhang, S. Yang, S. Qin, P. Wang, W. Wang, N. Mitsuzaki, Z. Chen, Effects of DPS on surface roughness and mechanical properties of electrodeposited copper foils, Cryst. Res. Technol. 58 (10) (2023) 2200260.
[44] S. Yang, W.-C. Wang, R. Zhang, S.-P. Qin, M.-X. Wu, N. Mitsuzaki, Z.-D. Chen, Effect of sodium alcohol thiyl propane sulfonate on electrolysis of high performance copper foil for lithium ion batteries, J. Electrochem. 28 (6) (2022) 5.
[45] S. Zhang, M. Sakane, T. Nagasawa, K. Kobayashi, Mechanical properties of copper thin films used in electronic devices, Procedia Eng 10 (2011) 1497–1502.
[46] T. Jacobsen, K. West, Diffusion impedance in planar, cylindrical and spherical symmetry, Electrochim. Acta 40 (2) (1995) 255–262.
[47] A. Siwach, P.K. Verma, Synthesis and therapeutic potential of imidazole containing compounds, BMC Chem 15 (2021) 1–69.
[48] S. Chon, W.-k. Paik, Adsorption of self-assembling sulfur compounds through electrochemical reactions: effects of potential, acid and oxidizing agents, Phys. Chem. Chem. Phys. 3 (16) (2001) 3405–3410.
[49] J.B. Schlenoff, M. Li, H. Ly, Stability and self-exchange in alkanethiol monolayers, J. Am. Chem. Soc. 117 (50) (1995) 12528–12536.
[50] D. Grujicic, B. Pesic, Electrodeposition of copper: the nucleation mechanisms, Electrochim. Acta 47 (18) (2002) 2901–2912.
[51] R. Li, X. Zhang, H. Dong, Q. Li, Z. Shuai, W. Hu, Gibbs–Curie–Wulff theorem in organic materials: a case study on the relationship between surface energy and crystal growth, Adv. Mater. 28 (8) (2016) 1697–1702.
[52] S. Kondo, T. Mitsuma, N. Shibata, Y. Ikuhara, Direct observation of individual dislocation interaction processes with grain boundaries, Sci. Adv. 2 (11) (2016) e1501926.
[53] J. Kacher, B. Eftink, B. Cui, I. Robertson, Dislocation interactions with grain boundaries, Curr. Opin. Solid State Mater. Sci. 18 (4) (2014) 227–243.
[54] L. Lu, X. Chen, X. Huang, K. Lu, Revealing the maximum strength in nanotwinned copper, Science 323 (5914) (2009) 607–610.
[55] Z. Cheng, H. Zhou, Q. Lu, H. Gao, L. Lu, Extra strengthening and work hardening in gradient nanotwinned metals, Science 362 (6414) (2018) eaau1925.
[56] Y. Zhang, J. Wang, N. Tao, Tensile ductility and deformation mechanisms of a nanotwinned 316L austenitic stainless steel, J. Mater. Sci. Technol. 36 (2020) 65–69.
[57] L. Lu, Y. Shen, X. Chen, L. Qian, K. Lu, Ultrahigh strength and high electrical conductivity in copper, Science 304 (5669) (2004) 422–426.
[58] B. Hanna, S. Lee, T. Brink, M. Ghidelli, G. Dehm, Understanding grain boundary electrical resistivity in Cu: the effect of boundary structure, ACS nano 15 (10) (2021) 16607–16615.
[59] K. Lu, Stabilizing nanostructures in metals using grain and twin boundary architectures, Nat. Rev. Mater. 1 (5) (2016) 1–13.
[60] R. Schmelzle, B. Giakupian, T. Muschik, W. Gust, R. Fournelle, Diffusion induced grain boundary migration of symmetric and asymmetric< 011>{011} tilt boundaries during the diffusion of Zn into Cu, Acta Mater 40 (5) (1992) 997–1007.